https://doi.org/10.1016/j.cemconcomp.2022.104834

Development of artificial geopolymer aggregates with thermal energy storage capacity

Yi Fang[a, b], Muhammad Riaz Ahmad[b], Jian-Cong Lao[b], Lan-Ping Qian[b], Jian-Guo Dai[b, *]

[a] *College of Mechanics and Materials, Hohai University, Nanjing, Jiangsu 211100, P.R. China*

[b] *Department of Civil and Environmental Engineering, The Hong Kong Polytechnic University, Kowloon, Hong Kong*

Abstract

Integrating phase change materials (PCMs) into building materials has been widely used to improve the energy efficiency of buildings, in which microencapsulation and shape stabilization of PCMs are considered as two most effective solutions. In this study, artificial geopolymer aggregate (GPA) was employed as a novel PCM carrier for energy storage purposes. Detailed investigations were conducted into the physical, mechanical, and thermal properties of GPA-PCM, which can be engineered through different raw material selections (e.g., slag content, water/binder ratio, and incineration bottom ash (IBA) content). It was demonstrated that increasing the IBA content is an efficient means to increase the porosity of GPA, an index of the capacity to accommodate PCM. Up to 16 wt.% PCM could be absorbed into the GPA through vacuum suction, resulting in a significant melting enthalpy of 24.74 J/g. Besides, GPA-PCM could achieve an excellent mechanical strength greater than 53.2 MPa and thermal conductivity of 0.510 – 0.589 W/mK. The time-temperature history curves of GPA revealed that up to 10.5°C of thermal regulation was achieved due to PCM impregnation. The developed GPA-PCM composites facilitate an innovative and low-carbon solution for utilizing PCMs in construction for temperature-regulating and energy-saving purposes.

* Corresponding author. Tel.: +85227666026. Email address: cejgdai@polyu.edu.hk (J. Dai)

Keywords: Phase change materials; Artificial geopolymer aggregates; Energy storage; Thermal performance; Mechanical properties

1 Introduction

Buildings account for at least 40% of overall worldwide energy consumption [1] and 28% of total annual CO_2 emission [2] due to the consumption of fossil fuels. To cope with this challenging scenario, the energy efficiency of buildings needs to be improved with unremitting efforts, which would reduce not only the living cost but also the environmental impact of energy consumption. Integrating phase change materials (PCMs) into building materials has been widely used to address the above challenge since PCMs can improve the energy efficiency of buildings through Thermal Energy Storage (TES) and thermal regulation [3]. PCMs, undergo phase transitions from solid to liquid and vice versa at their phase transition temperatures, along with absorbing or releasing a large amount of energy. PCM-enhanced building envelopes have been studied to narrow the gap between the peak and off-peak loads, save building operation costs under specific electricity tariffs, reduce diurnal temperature fluctuations concerning the occupants' thermal comfort, utilize the free cooling at night for save the day peak cooling load, etc. [4-7]. Besides, PCMs could modify the release process of the hydration heat of cementitious materials and relieve the temperature fluctuations to reduce shrinkage and cracks, thus improving the strength and durability of building materials [7].

Extensive existing studies [8, 9] have demonstrated that using PCMs can achieve significant energy savings for buildings. A recent study in Oak Ridge National Laboratory (ORNL) indicated that the PCM-integrated wallboard could produce up to 22% electricity savings from the wall-generated cooling loads [9]. However, the leakage of PCMs from the building material during the solid-liquid phase change processes is the major limitation of their applications [10]. To address this issue, there have been considerable efforts devoted to incorporating PCMs into construction materials, among which microencapsulation of PCMs in

suitable wall materials and shape stabilization of PCMs with various supporting materials are the two most effective solutions, as shown in Fig. 1. Currently available microcapsules of PCMs often break easily when they collide with each other [11]. The shell of microcapsules could be destroyed by the collision and abrasion with other aggregates during the mixing process and by the high pH environment of the cement hydration system [12]. Therefore, they are not favored for use in building materials that require high strength, such as concrete. Besides, the production cost of PCM micro-encapsulates is much higher (about seven times) compared to the non-encapsulated approach [13]. On the other hand, to overcome the above-mentioned disadvantages of microencapsulation, supporting materials can be added to PCMs to produce shape-stabilized PCMs or form-stable composite PCMs [14-16]. In this way, PCMs are absorbed into porous supporting materials via vacuum impregnation or direct absorption. Comparatively, the shape-stabilized approach is an easy, suitable, and economic pathway for the application of PCMs in buildings. Various types of porous materials, including expanded graphite [17], expanded perlite [18], expanded shale [19], mesoporous zeolite [20], ceramic foam [21], and recycled expanded glass aggregate [22] have been reported for such purpose. However, the cost of these porous supporting materials is relatively high and the mechanical properties are generally poor and their porosity is non-tuneable.

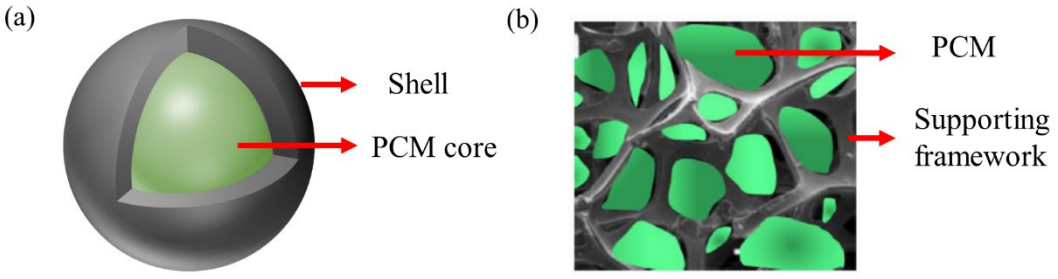

Fig. 1 Encapsulation methods of PCM: (a) microencapsulation; (b) shape-stabilization [23].

This study investigates the feasibility of employing artificial geopolymer aggregate (GPA) as a porous and designable carrier to fabricate form-stable PCMs composites. GPA is a type of

71 newly-developed porous alternative aggregate, which is produced from aluminosilicate-rich
72 sources via the alkali-activation method [24-27]. Usually, the produced GPAs could exhibit
73 more than 20% porosity yet reasonably high mechanical strength (e.g., 20 MPa for bulk
74 crushing strength). Commonly, with the increase of slag content and decrease of water to binder
75 ratio, the mechanical strength of GPA increases, while the porosity and water absorption rate
76 decrease [24, 25]. On the other hand, the use of pore-foaming agents can considerably increase
77 porosity, thus reducing the bulk density, thermal conductivity, and compressive strength.
78 Municipal solid waste incineration bottom ash (IBA) is a suitable natural foaming agent for
79 alkali-activated materials due to the production of hydrogen from the reaction of alkali and
80 residual aluminum metal particles in IBA [28]. In this way, sustainable and cost-effective
81 shaped-stabilized GPA-PCMs could be produced. Thus, the properties of GPA can be
82 manipulated based on selecting different portions of raw materials to achieve targeted porosity,
83 density, and mechanical strength.

84 In this study, shape-stabilized PCMs were prepared using a vacuum impregnation
85 technique. The effects of slag replacement content, water-to-binder ratio, and IBA content were
86 evaluated on the physical and mechanical properties of GPAs and GPA-PCMs, including the
87 specific gravity, water absorption, compressive strength, and crushing strength. Moreover, the
88 thermal properties, thermal stability, and thermal performance of GPA-PCMs were evaluated
89 using Thermogravimetric Analysis (TGA), Differential Scanning Calorimetry (DSC), thermal
90 conductivity, and thermal response via time-temperature history curves. Besides, three-
91 dimensional (3D) micro-CT was used to characterize the microstructures of GPA and GPA-
92 PCM.

2 Materials and Methods

2.1 Materials

In this study, FA was supplied by CLP Power Hong Kong Limited, while the ground granulated blast-furnace slag (GGBS) was purchased from Green Island Cement Co. Ltd., Hong Kong. The incineration bottom ash (IBA) was obtained from the Laogang Waste Incineration Power Plant in Shanghai, China. The oven-dried fine IBA aggregates with a size of <14 mm were ground with ball milling for several hours into fine powder. The chemical composition and loss on ignition (LOI) values of the FA, GGBS, and IBA were determined by X-ray Fluorescence (XRF), as shown in Table 1. The FA is classified as Class F according to ASTM C618-19 [29]. The particle size distribution of precursors was measured by a laser particle size analyzer, and the results are plotted in Fig. 2. The D_{50} particle size of FA, GGBS, and IBA was 17.99 μm, 12.37 μm, and 23.16 μm, respectively.

Industrial grade anhydrous sodium metasilicate (Na_2SiO_3-Anhydrous) in granules form was chosen as the solid alkaline activator [30], which was purchased from Qingdao Haiwan Chemical Co., Ltd. It contained 55.6% Na_2O, 43.7% SiO_2, and 0.7% impurities, thus having a modulus ratio (SiO_2/Na_2O) of 0.81. The Na_2SiO_3-Anhydrous had a D_{50} particle size of 241.16 μm, as shown in Fig. 2, and a loose bulk density of 1.31 g/cm^3.

Table 1 Chemical composition of precursors obtained from XRF (wt. %)

Oxides	SiO_2	Al_2O_3	CaO	Fe_2O_3	TiO_2	MgO	SO_3	Na_2O	K_2O	P_2O_5	Others	LOI
FA	47.5	26.1	5.85	9.63	1.12	2.72	1.57	2.48	2.02	0.65	0.36	3.48
GGBS	32.6	14.7	42.4	0.35	0.61	6.53	1.82	-	0.41	0.18	0.40	0.26
IBA	42.8	7.63	22.3	7.77	0.93	2.33	1.76	5.43	1.54	4.96	2.50	-

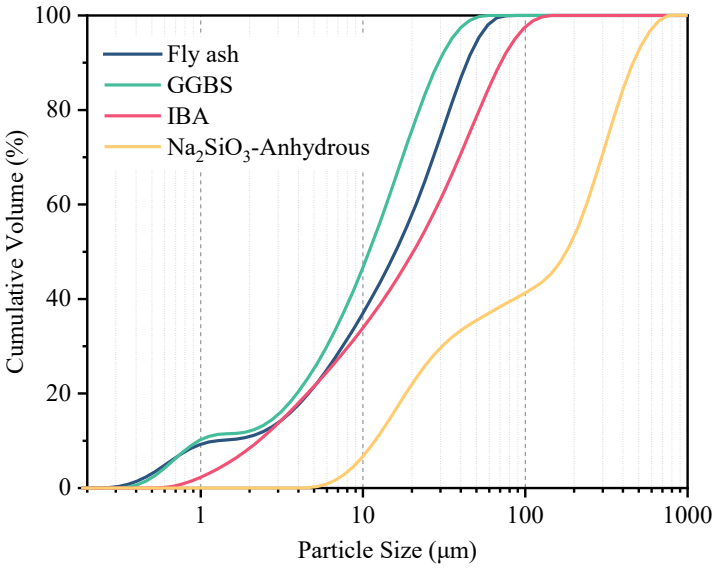

Fig. 2 Particle size distribution of FA, GGBS, IBA, and Na_2SiO_3-Anhydrous.

An industrial-grade paraffin wax, purchased from Joule Wax Co. Ltd in Shanghai, was chosen as the PCM in this study. Its phase transition temperature is 28°C. The apparent density for PCM in liquid and solid states is 0.80 g/cm^3 and 0.88 g/cm^3, respectively. The specific heat capacity and thermal conductivity of PCM are 3.22 J/(g·K) and 0.21 W/(m·K), respectively, as supplied by the producer. The thermal stability and thermal enthalpy are measured by TGA and DSC, respectively, as shown in Fig. 3. The melting and crystallization enthalpy for this type of paraffin wax was calculated as 250.1 J/g and 254.6 J/g, respectively. According to Fig. 3a, the PCM will start to decompose from 110°C and completely decomposes after 225°C, indicating good thermal stability for building applications.

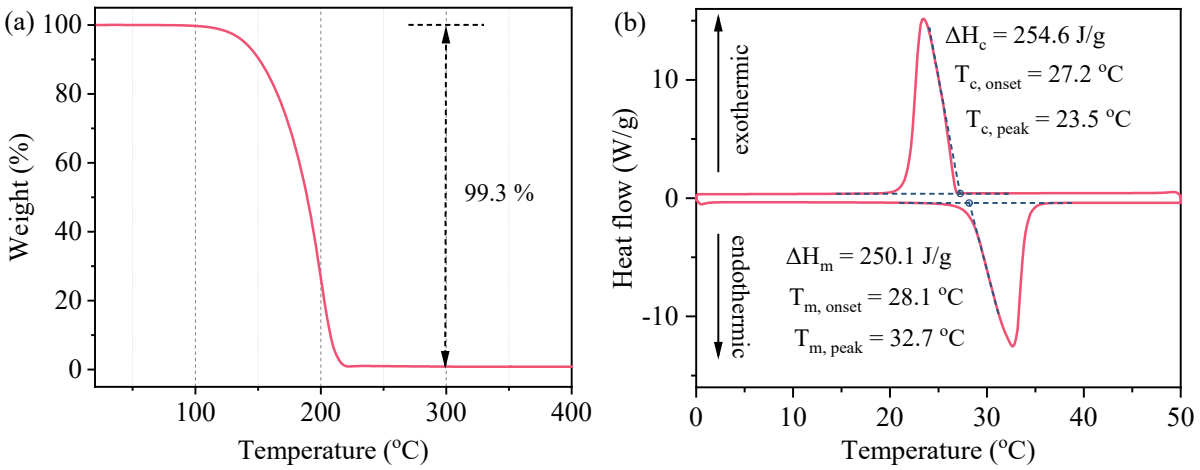

Fig. 3 Thermal performance of the PCM: (a) Thermal loss of PCM determined by TGA; (b) Thermal capacity and phase change temperatures determined by DSC.

2.2 Mix design

2.2.1 GPA production

To achieve different levels of porosity and mechanical properties of GPA, one-part geopolymer pastes were produced based on the three key factors: water/binder ratio, GGBS replacement ratio to FA, and IBA content, as shown in Table 2. There were three different water/binder ratios (0.25, 0.3, 0.35), GGBS replacement ratios (10%, 15%, 20%), and IBA contents (0, 2%, 5%), resulting in a total of seven types of geopolymer pastes. The mix ID was designated based on the above three factors.

Table 2 Mix proportions of one-part geopolymer pastes (by wt.)

Groups	FA	GGBS	IBA	Na_2SiO_3-Anhydrous	Water
10S-0.25	0.9	0.1	-	0.1	0.25
15S-0.25	0.85	0.15	-	0.1	0.25
20S-0.25	0.8	0.2	-	0.1	0.25
15S-0.35	0.85	0.15	-	0.1	0.35
15S-0.3	0.85	0.15	-	0.1	0.3
15S-0.3-2B	0.83	0.15	0.02	0.1	0.3
15S-0.3-5B	0.80	0.15	0.05	0.1	0.3

Following the procedures reported by Xu et. al (2021) for one-part geopolymer [25], the precursor materials and solid activators were dry-mixed for 5 mins, followed by mixing for another 5 mins after adding the water. The geopolymer samples were then cast into 70 mm × 70 mm × 70 mm cubic molds, placed at ambient temperature, and demoulded in 24h. After demoulding, half of the specimens were crushed using a compressive loading machine at a loading rate of 0.5 kN/s to obtain the one-day compressive strength. The broken specimens were further crushed by a hammer to obtain the coarse GPAs with sizes smaller than 20 mm. In this study, only the coarse GPAs with a size of 10 – 20 mm were used. All the aggregates and remaining cubic samples were cured in an oven for 24 hours at 105°C to mitigate the autogenous shrinkage [25] and accelerate the strength development. Then these samples were followed with another five days of sealed curing at room temperature. The properties of GPA and cubic samples were tested at 7d. The crushing strength of GPA was obtained by casting the samples into 20 mm × 20 mm × 20 mm cubes. The curing conditions were kept the same as that for the crushed GPAs.

2.2.2 Preparation of GPA filled with PCM (GPA-PCM)

The GPA-PCM was prepared via a vacuum impregnation process, as shown in Fig. 4. At first, 500 grams of oven-dried GPAs were weighed and placed into a covered container. The container was put in the water bath at 50°C and exposed to a vacuum pressure of approximately 85 kPa for 2 hours. The melted liquid PCM solution was then introduced into the container to submerge the GPA completely. The obtained mixture was kept in the vacuum at 50°C for another 10 hours. The completion of loading was achieved after removing the vacuum for another 2 hours of soaking. Then the mixtures were placed on a sieve to remove the extra liquid PCM, followed by immersion in cold water (~ 7°C) to freeze the inner PCM. Since the PCM residue on the GPA surface might affect the surface coating process of GPA-PCM, a warm water-rinsing method was used to remove the PCM film according to previous research [19].

After rinsing, the PCM residue on the surface of GPA-PCM could be effectively removed. Then the GPA-PCM was immersed in the cold water again and air-dried for 48 hours to remove the moisture before use. The mass of air-dried GPA-PCM was recorded to calculate the PCM absorption rate according to the mass change.

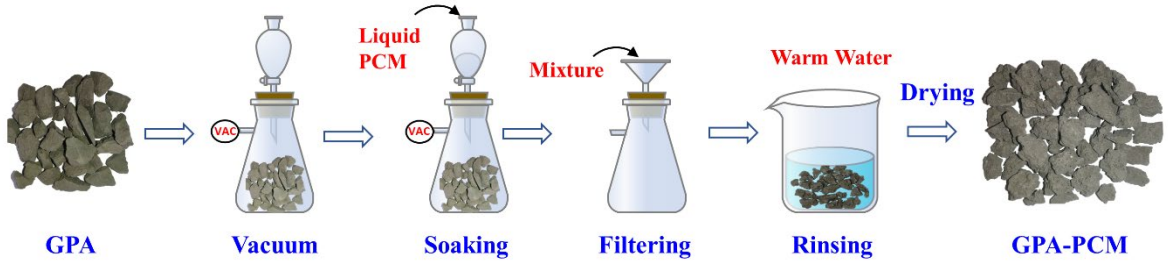

Fig. 4 Schematic illustration of the preparation process for GPA-PCM.

2.3 Characterization methods

2.3.1 Specific gravity, water absorption, and vacuum water absorption

Approximately 500 grams GPA with diameters of 10 – 20 mm were used in the specific gravity test [including bulk specific gravity (G_B), saturated surface dry specific gravity (G_{SSD}), and apparent specific gravity (G_A)] according to ASTM C128-15 [31] and C127-15 [32]. The aggregates were soaked in the water for 24 hours, followed by wiping with a burlap cloth to achieve a saturated surface dry (SSD) condition. The mass of SSD aggregates was recorded as m_{SSD}. Meanwhile, the mass of the pycnometer filled with water was recorded as m_{pyc}. Then the aggregates were put into the pycnometer, and the pycnometer was filled with water. The total weight of the pycnometer, water, and aggregates was recorded as $m_{pyc+aggr}$. Finally, the aggregates were taken out and placed in an oven (105°C) for 24 hours to achieve the oven-dry state. The mass of oven-dried aggregates was recorded as m_{OD}. For the specific gravity test of GPA-PCM, the oven-dry state was achieved by freeze-drying (Labconco FreeZone Benchtop Freeze Dryer) since the elevation of temperature could cause the melting of PCM, resulting in the leakage of PCM and unreliable results. The mass of final dry aggregates was still noted as

m_{OD}. Then the specific gravity (SG) and water absorption of aggregates are calculated by the following equations:

$$Bulk\ SG:\ G_B = \frac{m_{OD}}{m_{SSD} + m_{pyc} - m_{pyc+aggr}} \quad (1)$$

$$SSD\ SG:\ G_{SSD} = \frac{m_{SSD}}{m_{SSD} + m_{pyc} - m_{pyc+aggr}} \quad (2)$$

$$Apparent\ SG:\ G_A = \frac{m_{OD}}{m_{OD} + m_{pyc} - m_{pyc+aggr}} \quad (3)$$

$$Absorption\ rate\ (\%):\ S_w = \frac{m_{SSD} - m_{OD}}{m_{OD}} \times 100\% \quad (4)$$

For the vacuum water absorption test, the aggregates were vacuum saturated by a BSJ fully automatic saturation machine. The subsequent procedures in the vacuum saturation were the same as those used for the water absorption test. Then the vacuum absorption rate ($S_{v,\,w}$) could be obtained using Eq. (4). Compared with the regular water absorption test, the capillary pores in the geopolymer could be fully saturated under vacuum conditions within 24 hours of immersion. Thus, this index could also be used to determine the porosity of the pastes [33].

2.3.2 Compressive strength

The compressive strength of the 70 mm × 70 mm × 70 mm geopolymer cube samples was measured by a Matest Test Frames Group machine. All the groups were tested in triplicates at the ages of 1d and 7d according to ASTM C109 at a loading rate of 0.6 MPa/s [34, 35].

The crushing strength of GPA was determined by testing the compressive strengths of 20 mm × 20 mm × 20 mm cubes by a Testometric X500-50 machine with a 50 kN capacity according to our previous research [26, 27]. The average crushing strength was obtained by testing six samples before and after encapsulating with PCM according to ASTM C109 [34]. The loading rate to determine the crushing strength was 0.5 mm/min.

206 *2.3.3 Thermogravimetric analysis (TGA)*

207 GPA and GPA-PCM samples (around 20 g) were dried in a vacuum oven, crushed, and
208 ground into fine powders. The ground powders were then sieved through the #200 mesh size
209 (75 μm) for TGA or DSC measurements [36]. Approximately 10 mg of each sample was
210 weighed into an aluminate crucible for TGA analysis, and samples were tested with a Rigaku
211 Thermo Plus EVO2 instrument. For each test, the sample was first held at 23°C for 30 min and
212 then heated from 23°C to 500°C at 10°C /min under N_2 purge with a flow rate of 100 mL/min.

213 *2.3.4 Differential scanning calorimetry (DSC)*

214 The phase change temperature and latent heat of the GPA-PCM fine powers were
215 measured using a differential scanning calorimeter (DSC3, Mettler Toledo). For DSC
216 measurements, around 6 mg of each sample was sealed in an aluminum crucible with a lid for
217 characterization at a heating and cooling rate of 10°C/min and under a nitrogen atmosphere
218 with a flow rate of 50 mL/min [37]. The samples were cooled from 50°C to 0°C and then heated
219 from 0°C to 50°C.

220 *2.3.5 Thermal conductivity*

221 The thermal conductivity of GPA and GPA-PCM was measured using a TC3000E thermal
222 conductivity meter based on the principle of the transient hotwire method [38] at room
223 temperature (21.5°C). Due to the size limit of transducers (~30 mm × 45 mm), six samples of
224 geopolymer cubes (50 mm × 50 mm × 50 mm) for each group were produced and cured under
225 the same conditions with GPA. Before the test, the geopolymer cubes were completely dried in
226 the oven. The connecting surfaces of the two samples were kept smooth to obtain precise results
227 [39]. After encapsulating with PCM, the same cubes were air-dried at room temperature for 48
228 hours, followed by another batch of thermal conductivity tests. Three samples for each group
229 were tested to report the average thermal conductivity, and all measurements were conducted
230 at a fixed voltage of 2 V.

2.3.6 Time-temperature history

Thermal response and regulation of GPA-PCM were evaluated by time-temperature history curves [40, 41], in which the temperature was recorded by embedding the thermocouples into the samples. The curing conditions for these GPA-PCM cubes were the same as those for GPA. Half of the cubes embedded with thermocouples were encapsulated with PCM via vacuum impregnation. A light heater with a 500W halogen lamp was located 40 cm above the center of samples, as shown in Fig. 5a. GPA and GPA-PCM samples were arranged as shown in Fig. 5b. The tested samples could receive a light intensity of around 11000 Lux based on the lab measurements. The temperature data logger was HIOKI LR8431 Memory HiLoggers, and the type of thermocouples was KPS-TT-K-24. The samples were heated to 50°C with the light on for 1 hour, then cooled to room temperature (21.5°C) with the light off for 1.5 hours.

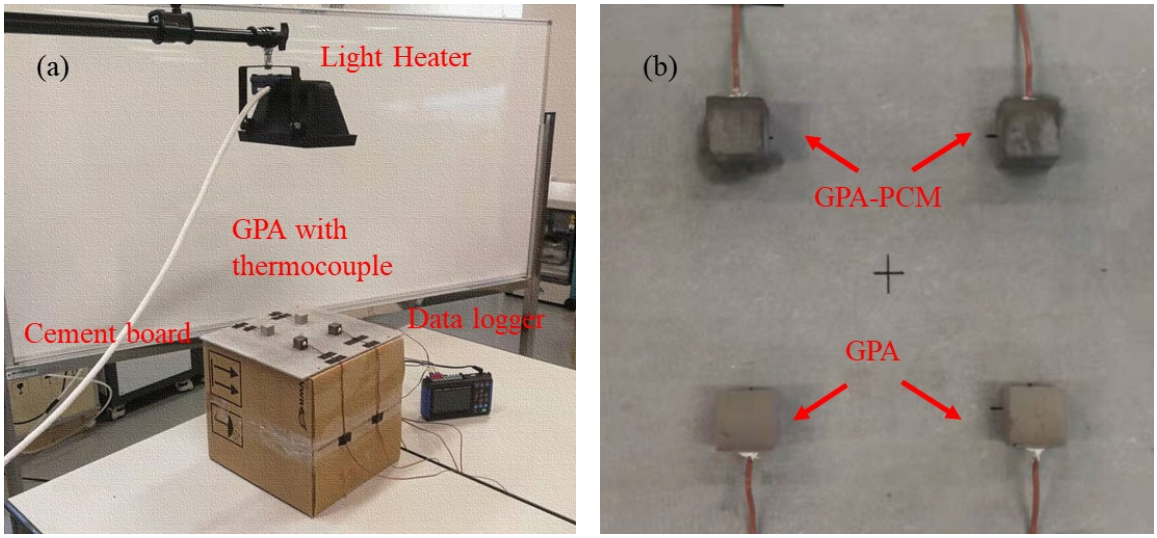

Fig. 5 Experimental setup of the time-temperature curve: (a) Schematic layout; (b) Sample arrangements.

2.3.7 Micro X-ray microtomography (Micro-CT)

The 3D X-ray micro-CT images of microstructure for the GPA and GPA-PCM samples were observed with Bruker Skyscan 1276 Micro-CT at 100 kV and 200 μA. The crushed

250 artificial geopolymer aggregates and the aggregates filled with PCM with an irregular shape
251 between 14-20 mm were used for the micro-CT scanning. To capture the distribution of the
252 pores and solid paraffin wax in GPA-PCM, the resolution for the micro-CT scanning was set
253 as 14 μm. The final reconstructed cylinder size was selected as 12 mm diameter by 10 mm
254 height.

255 **3 Results and Discussions**

256 **3.1 Physical properties of GPA and GPA-PCM composites**

257 *3.1.1 Specific gravity*

258 Fig. 6 shows the specific gravities of GPA and GPA-PCM composites regarding the three
259 factors: slag content, water content, and IBA content. As shown in Fig. 6a, the influence of slag
260 content and water-to-binder ratio was minimal on the apparent specific gravity (G_A) of
261 produced GPA. However, the G_A gradually decreased with the increase in the content of IBA.
262 This is because the alumina in IBA could react with alkali and generate hydrogen gas, thus
263 producing more isolated entrained air voids in the pastes. After encapsulation with PCM, the
264 G_A of aggregates was reduced due to the relatively low density of PCM stored in the open pores
265 of GPA. The overall trend of variation in G_A of GPA was similar before and after the
266 encapsulation.

267 Fig. 6b presents the SSD specific gravity (G_{SSD}) of GPA and aggregates filled with PCM.
268 It could be seen that the trend of G_{SSD} was related to the selected three key parameters: slag
269 content, water content, and IBA content. Higher slag replacement could cause an increase in
270 the G_{SSD}, while an increase in water content and IBA content could lower the G_{SSD} of GPA.
271 The G_{SSD} value was slightly reduced after encapsulation of GPA with PCM due to the lower
272 solid density of PCM compared with water.

273 The bulk dry specific gravity (G_B) of GPA and GPA-PCM is shown in Fig. 6c. Before
274 being loaded with PCM, the overall trend of G_B and G_{SSD} was similar. The G_B of GPA varied

in the range of 1.52 to 1.78, which is much lower than that of natural aggregates (2.69). Thus, GPA falls in the category of lightweight aggregates. However, the encapsulation of PCM increased the value of G_B due to the filling of pores. Compared with the other two factors, the addition of IBA could generate more pores and lead to the formation of GPA with lower density. As a result, 15S-0.3-5B achieved the lowest apparent (G_A), SSD (G_{SSD}), and bulk specific gravity (G_B) before and after encapsulation.

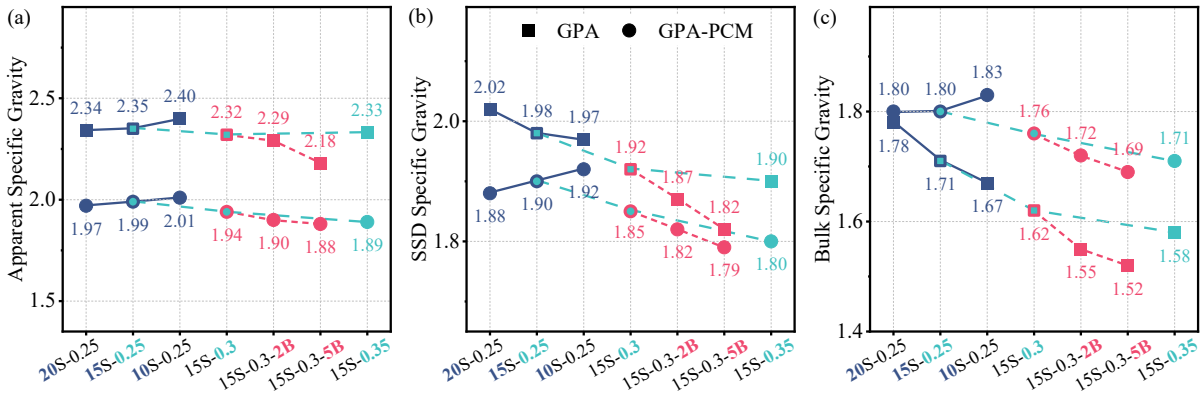

Fig. 6 Specific gravity of GPA and GPA-PCM: (a) Apparent specific gravity; (b) SSD specific gravity; and (c) Bulk dry specific gravity.

3.1.2 Water absorption

The water absorption results of GPA and GPA-PCM are shown in Fig. 7. Without loading with PCM, the produced artificial aggregates had a water absorption (13 - 21%) significantly higher than the natural limestone aggregates (2%). The lower content of slag, higher water-to-binder ratio, and higher IBA content resulted in a more porous structure and lower density, which in turn increased the water absorption of GPA. As a result, group 15S-0.3-5B had the highest water absorption (21%), which is consistent with the aforementioned results of specific gravity. Due to the high-water absorption characteristics of GPA, the inner pores could be utilized for thermal energy storage.

After being filled with PCM via vacuum impregnation, water absorption of the GPA-PCM was significantly reduced due to the filling of the open pores and the hydrophobic properties

of paraffin wax. The highest reduction in water absorption of 73.95% was observed for group 15S-0.3-5B, which corroborates the results of the highest water absorption before encapsulation. It is worth mentioning that the water absorption of all groups was quite close to each other and was around 5.50%. The lower water absorption of GPA-PCM could avoid the negative effects on concrete durability properties such as freeze-thaw resistance [25]. Therefore, the impregnation of PCM into GPA could not only store thermal energy but also reduce water absorption to a tolerable limit (around 5%).

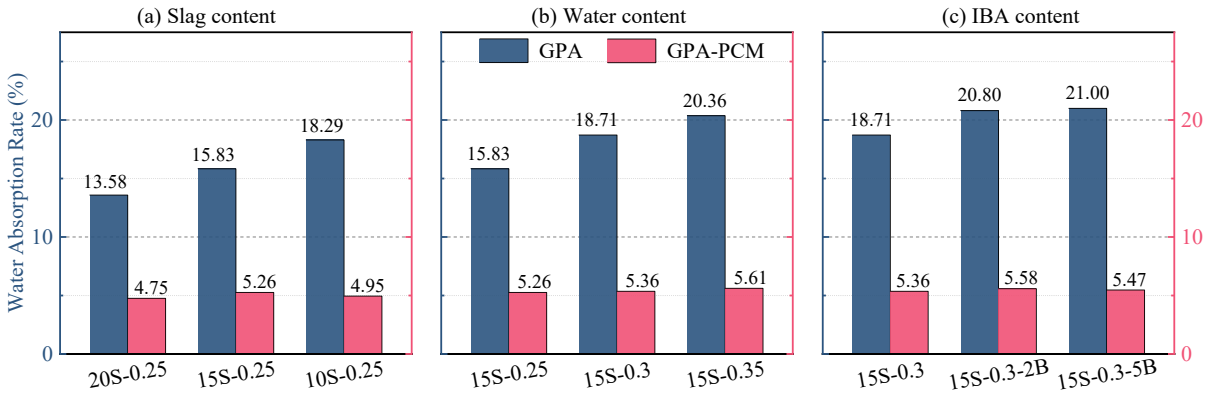

Fig. 7 Water absorption rate of GPA and GPA-PCM affected by: (a) Slag content; (b) Wate content; and (c) IBA content.

3.1.3 Porosity and PCM absorption rate

In order to estimate the overall porosity of GPA, the vacuum water absorption rate of the produced GPA was measured, and the results are presented in Fig. 8. The lower slag addition, higher water-to-binder ratio, and more IBA resulted in a more porous structure. Regarding the pore-forming effect, IBA content had a more significant effect over the other two parameters. This is understandable because the addition of IBA generates much more macro-pores due to the release of hydrogen gas.

The high intrinsic porosity of GPA allows it to serve as a PCM carrier. After the vacuum impregnation of PCM, the mass change rate of the GPA was recorded and noted as the PCM absorption rate, as shown in Fig. 8. The addition of IBA was a more efficient strategy to

promote the PCM absorption into GPA as compared with the adjustment of slag and water content. This is because the air voids generated by IBA were much easier to be filled by the liquid PCM under vacuum conditions due to the low pore pressure. For a given liquid, there is a higher capillary force for the smaller pores, according to the Young-Laplace equation [19]. As a result, group 15S-0.3-5B achieved the highest absorption rate of PCM, which was up to 15.99 wt. %.

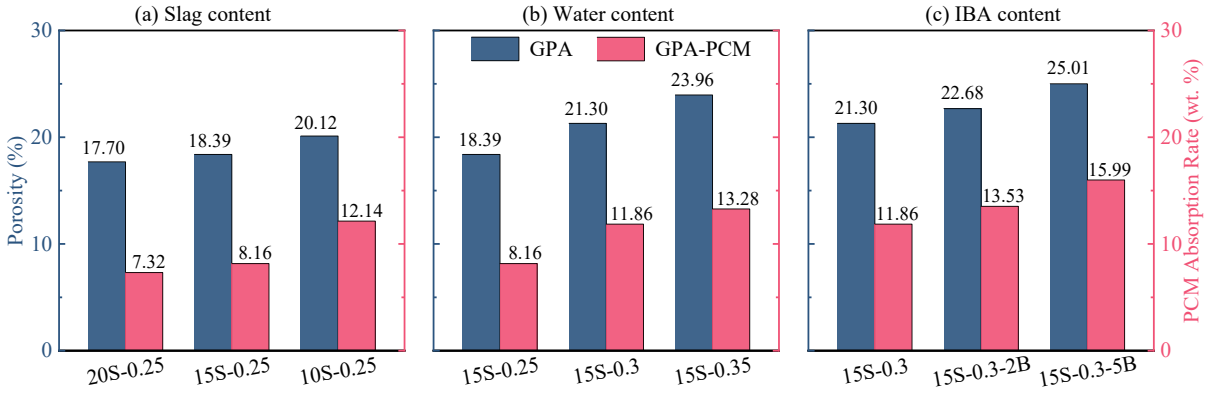

Fig. 8 Porosity of GPA and absorption rate of PCM in GPA-PCM affected by: (a) Slag content; (b) Wate content; and (c) IBA content.

3.2 Mechanical properties of GPA and GPA-PCM composites

3.2.1 Compressive strength

Fig. 9 presents the compressive strength of geopolymer pastes at 1d and 7d. The 1d compressive strength relates to the crushing energy of the produced GPA, and the higher early strength means more energy is required for the crushing process. After 24 hours of heat curing and 5d extra ambient temperature curing, the compressive strength of geopolymer at 7d could be considered as the long-term strength [42], which reflects the service mechanical performance of the produced GPA and GPA-PCM. According to Fig. 9, the 1d compressive strength had a positive relationship with the increase in slag content and an inverse relationship with the increase in water content and IBA content. The highest compressive strength of 19.8 MPa at 1d was observed for the group containing 20% slag. In addition, the compressive

strength of 20S-0.25 at 1d was about twice higher than that of 15S-0.25, however, the difference between their compressive strengths at 7d was significantly reduced. Similar results have been also reported in previous research on fly ash/ slag blended geopolymer [43, 44]. The higher early strength can be explained by the quick reaction of calcium compounds and high amorphous degree present in the slag. It should be mentioned that in the second group, the higher water-to-binder ratio in group 15S-0.35 induced a relatively higher early strength as compared to 15S-0.3. This could be associated with the higher amount of dissolution of solid alkaline-activator during the mixing process of one-part geopolymer. The addition of IBA could impair the early strength due to the increase in air voids, which is consistent with the high porosity shown in Fig. 8. As a result, group 15S-0.3-5B had the minimum early strength (1.4 MPa), which indicates it requires the minimum crushing energy in industrial production as compared to other groups.

The trend of 7d compressive strength was similar to that of 1d strength, except the group 15S-0.35, which is consistent with the porosity results shown in Fig. 8. As shown in Fig. 9, the addition of IBA had a much more negative effect on the 7d compressive strength compared with other two parameters. Thus, the minimum compressive strengths at 7d were 36.4 MPa for the group 15S-0.3-5B.

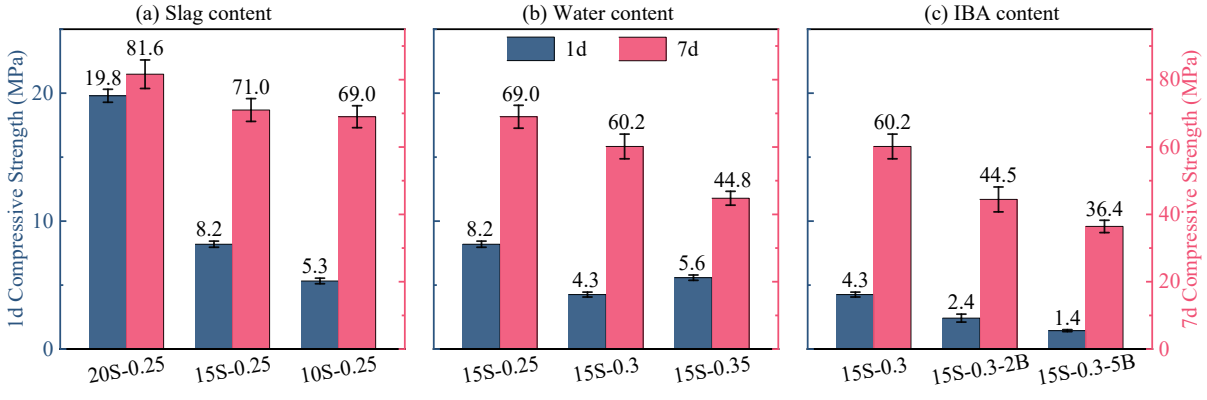

Fig. 9 Compressive strength of cubic geopolymer paste (70 × 70 × 70 mm^3) at 1d and 7d (after heat curing).

359 *3.2.2 Crushing strength*

360 In order to evaluate the strength of artificial aggregates at service life, the compressive
361 strength of the regular cubic aggregates (20 mm × 20 mm × 20 mm) was measured to reflect
362 the crushing strength of the GPA before and after encapsulating with PCM, as shown in Fig.
363 10. Since the porosity of the GPA was linearly influenced by the content of slag, water, and
364 IBA, the corresponding crushing strength had the same trend as the compressive strength, as
365 observed in Fig. 9. Due to the size effect in the cubic compressive strength [45], the crushing
366 strength of GPA was much higher (in the range of 17 - 60%) than the compressive strength of
367 cube geopolymer pastes. The mechanism of the size effect can be attributed to the stress
368 redistribution and energy release in the quasi-brittle materials [45]. The size effect was more
369 obvious in the porous aggregates like 15S-0.35 or 15S-0.3-5B. This feature benefits the
370 application of encapsulation of PCM in GPA for the following reasons. Firstly, in order to
371 increase the energy storage capacity, artificial aggregates require a higher porous structure,
372 which might sacrifice the overall strength of the concrete containing the GPA-PCM. However,
373 the size effect could provide strength compensation for GPA to achieve the balance of high
374 energy storage capacity and desirable strength. As a result, sample 20S-0.25 achieved the
375 highest crushing strength of 95.7 MPa, while 15S-0.3-5B still had a desirable crushing strength
376 of 58.2 MPa.

377 Besides the crushing strength of cubic GPA, the crushing strength of aggregates after
378 being filled with PCM via vacuum impregnation was also investigated. Compared with the
379 aggregates without PCM, the crushing strength of each group was decreased to varying extents.
380 The decrease in strength is attributed to the increase of microcracks during the vacuum
381 impregnation process, especially for cold-water bathing and warm-water rinsing. The large
382 temperature gradients generate thermal stress, and there is dilatation stress associated with the
383 phase transformation. Importantly, the strength loss is significantly related to the crushing

strength of GPA without being filled with PCM. The denser microstructure in GPA leads to a higher strength loss and vice versa. This degradation behavior might be explained by the fact that finer pores generate relatively high pore pressure, as well as higher dilatation and shrinkage stress associated with the phase transition. As a result, the GPA with the denser microstructure (20S-0.25) had the maximum strength loss.

It is worth noting that the trend of crushing strength of GPA-PCM was significantly different from that of the GPA regarding the three key parameters: slag content, water-to-binder ratio, and foaming agent content. The crushing strength of GPA-PCM for the group containing different slag contents was slightly increased. The water-to-binder ratio still governed the crushing strength of GPA-PCM, and the lower water content led to higher crush strength. For the group with varied IBA contents, the difference in the crushing strength of GPA-PCM was curtailed compared with that in GPA. That means the addition of a foaming agent significantly mitigated the thermal stress and dilatation stress during the vacuum impregnation process. It also explains why group 15S-0.3-5B not only had the maximum PCM absorption (15.99 wt.%) but also possessed a desired crushing strength (54.5 MPa).

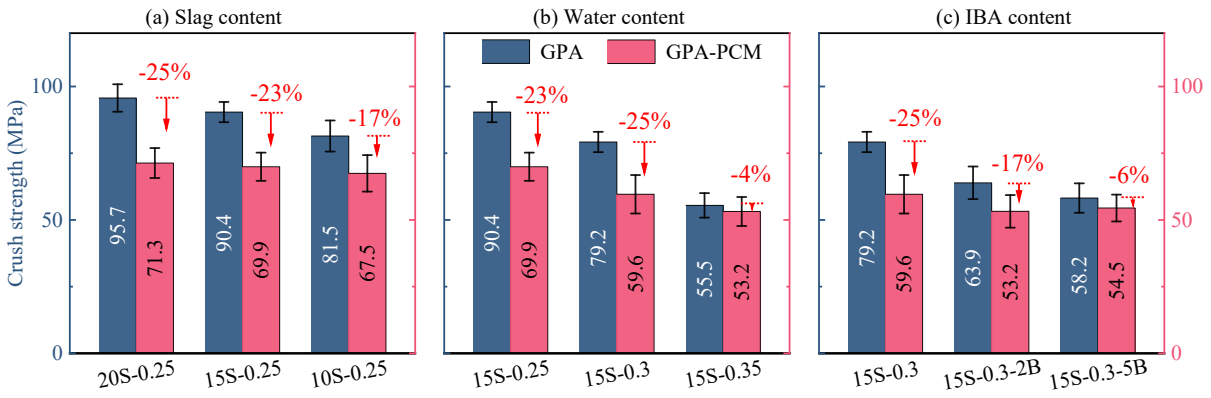

Fig. 10 Crushing strength of aggregates with the regular size of 20 mm × 20 mm × 20 mm before and after being filled with PCM.

3.3 Thermal properties of GPA-PCM composites

3.3.1 Thermal stability and storage capacity

Thermal stability is used to evaluate the adaptive ability of temperature changes during the application of GPA-PCM composites. Therefore, TGA was conducted to measure the stability of GPA-PCM during the continuous heating-up process [46]. As shown in Fig. 11, all the groups underwent mass loss (≈5%) up to 400°C; however, the difference in mass loss between the groups was not significant. For the GPA-PCM composites, additional mass loss was observed apart from the mass loss of GPA itself, as observed in Fig. 11a. The main mass loss occurred between 110°C and 215°C, which is consistent with the decomposition temperature interval of pure PCM (110 – 225°C) shown in Fig. 3. This indicates that the GPA-PCM has relatively good thermal stability.

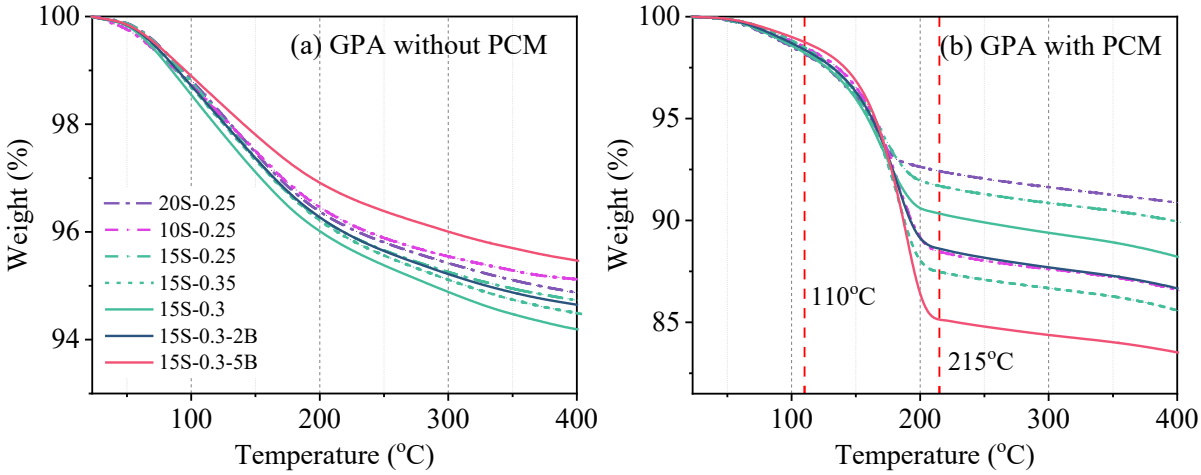

Fig. 11 TGA curves of GPA (a) and GPA-PCM (b).

Besides the thermal stability, the TGA results could also be used to measure the absorption capacity of PCM. Since GPAs could lose bonding water during the temperature elevation and PCM would fully decompose after 225°C, the actual weight of PCM in the GPA-PCM (R_{PCM}) could be calculated based on the following equations:

$$R_{PCM}\ (\text{wt. \%}) = (1 - \frac{m_{GPA-PCM@400}}{m_{GPA-PCM@23}} \times \frac{m_{GPA@23}}{m_{GPA@400}}) \times 100\% \quad (5)$$

where $m_{GPA@23}$ and $m_{GPA@400}$ are the mass of GPA at 23°C and 400°C, respectively; $m_{GPA-PCM@23}$ and $m_{GPA-PCM@400}$ are the mass of GPA-PCM at 23°C and 400°C, respectively.

The calculated results from TGA, as well as the direct mass change obtained in Fig. 8, were compared in Fig. 12a. It is shown that the PCM absorption rate obtained from TGA was lower than the PCM absorption obtained from the direct mass measurement. This is attributed to the inhomogeneous nature and small sample size (5 - 8 mg) of GPA-PCM used for TGA analysis. Besides, there was part of the inevitable loss of paraffin during the sample preparation process, such as PCM residue left on the surface of the grinding mortar and evaporation of paraffin [47]. Both methods showed that the PCM absorption increased with the water content and IBA content while decreasing with the increase in slag content.

The absorption efficiency of PCM was defined to describe the utilization rate of pores in GPA. It could be calculated based on the solid density of PCM (0.88 g/cm^3) and the vacuum water absorption ($S_{v,w}$) of GPA as follows, and the results are shown in Fig. 12b.

$$Absorption\ efficiency = \frac{PCM\ absorption\ capacity}{\rho_{PCM,Solid} / \rho_{water} \cdot S_{v,w}} \quad (6)$$

It was observed that GPA with a higher porous structure achieved higher absorption efficiency of PCM after vacuum impregnation. This was attributed to the presence of larger size pores in the highly porous structure of GPA, for which lower capillary force was required to fill the pores under the constant vacuum pressure. More importantly, an increase in the content of the foaming agent IBA could achieve a superior absorption efficiency as compared to an increase in water content. According to the direct estimation, the highest absorption efficiency of 72.66% was achieved by the group containing 5% IBA (15S-0.3-5B), whereas the lowest absorption efficiency of 47.0% was observed for the group containing 20% slag (20S-0.25). Besides, there was around 10% volume expansion or shrinkage due to the phase

transition of PCM. Consequently, the mentioned absorption efficiency was actually underestimated by about 10% when the paraffin transferred into the liquid state.

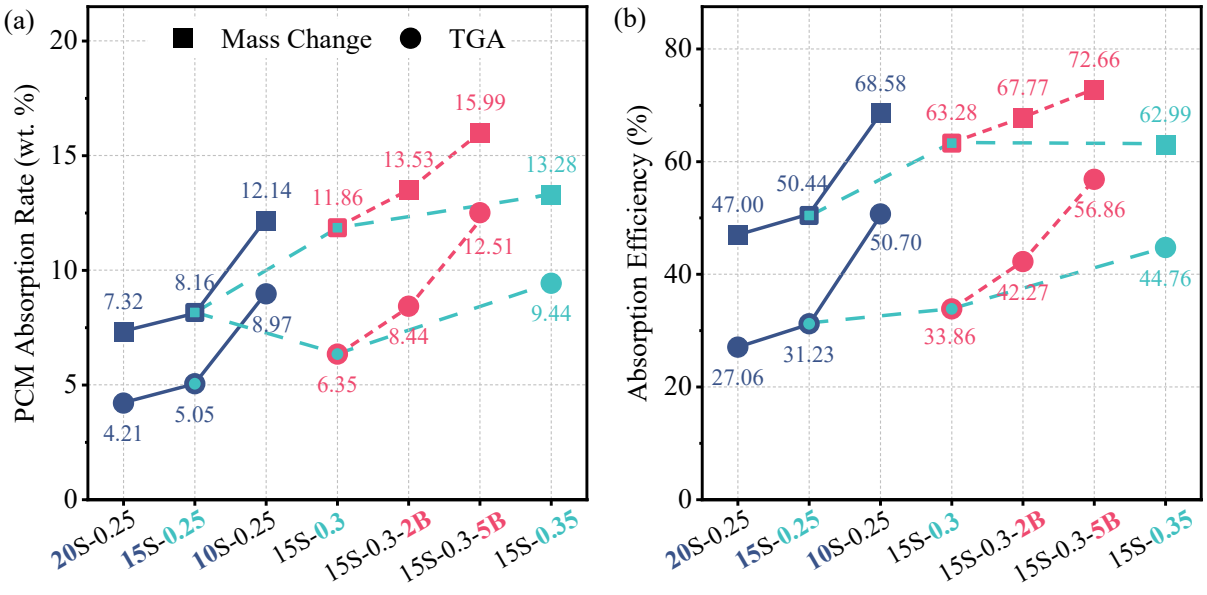

Fig. 12 PCM absorption rate estimated from the mass change and TGA method (a); and the corresponding absorption efficiency of PCM (b).

3.3.2 Latent heat

DSC was performed to determine the latent heat of prepared GPA-PCM composites, and the results are shown in Fig. 13. The details of onset phase change temperature (T_{onset}), peak temperature (T_{peak}), and latent heat of GPA-PCM and paraffin are concluded in Table 3. It can be seen that in comparison with the pure PCM, the phase change temperatures of GPA-PCM, including the onset and peak temperatures, were slightly shifted. This was probably attributed to the physical interactions between pore-confined paraffin and surrounding supporting materials [41, 47]. Besides, according to the Gibbs-Thompson equation [48], the melting or crystallization temperature of paraffin located in the pores decreases with the pore size. This is well verified by the DSC curves of the samples containing IBA. Unlike the other groups, the T_{onset} and T_{peak} of 15S-0.3-2B and 15S-0.3-5B were closer to those of paraffin itself due to the larger pore size.

According to Table 3, the latent heat of GPA-PCM increased with the increase in water and IBA content and decreased with the increase in slag content, which is consistent with the TGA results. The addition of IBA significantly improved the latent heat of the produced GPA-PCM, leading to the highest average enthalpy up to 24.11 J/g. Considering that the latent heat of GPA-PCM is positively correlated with the mass fraction of PCM, the PCM absorption capacity could be calculated as 9.55 wt. % for 15S-0.3-5B. This is quite close to the value obtained from TGA (12.51 wt. %).

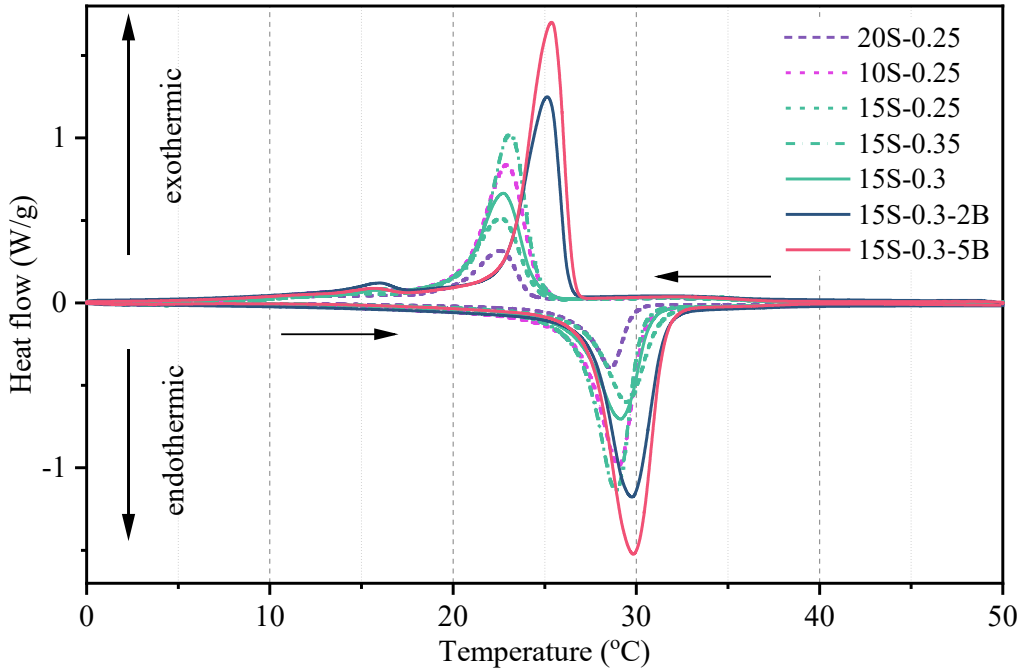

Fig. 13 DSC curves of GPA-PCM.

Table 3 Thermal enthalpy and onset temperature for the crystallization and melting process of GPA-PCM and PCM

Groups	Crystallization process			Melting process			Average enthalpy (J/g)
	T_{onset} (°C)	T_{peak} (°C)	Enthalpy (J/g)	T_{onset} (°C)	T_{peak} (°C)	Enthalpy (J/g)	
Paraffin	27.21	23.50	254.59	28.12	32.67	250.07	252.33
20S-0.25	24.26	22.53	4.65	26.53	28.50	4.29	4.47
10S-0.25	24.81	22.83	13.35	26.53	29.00	13.08	13.22

15S-0.25	24.62	22.58	8.95	26.90	29.33	9.77	9.36
15S-0.35	24.62	23.08	14.81	26.56	28.83	14.78	14.80
15S-0.3	24.62	22.75	10.33	26.40	29.17	11.35	10.84
15S-0.3-2B	26.34	25.17	17.28	27.27	29.83	18.00	17.64
15S-0.3-5B	26.63	25.33	23.47	27.27	29.83	24.74	24.11

475

476 *3.3.3 Thermal conductivity*

477 Thermal conductivity plays a key role in the heat transfer process and is dominantly
478 affected by the bulk dry density and the pore structure [49] of a material. As shown in Fig. 14,
479 the thermal conductivity of GPA had the same trend as the bulk density (Fig. 6c). The measured
480 value for GPA was between 0.409 W/mK and 0.523 W/mK, which is rated as an insulation
481 material according to RILEM's criterion (0.75 W/mK) [50]. The thermal conductivity of GPA
482 decreased with the increase in water and IBA content, while it reduced with the increase in slag
483 content. The decrease in thermal conductivity in groups containing different water and IBA
484 contents is due to the formation of a higher porous structure. However, a higher amount of slag
485 tends to form more amount of reaction products in GPA, leading to a denser microstructure
486 and increased thermal conductivity.

487 After being impregnated with PCM, the thermal conductivity of GPA was slightly
488 increased due to the filling of pores, and still lower than RILEM's criterion for insulation
489 materials. Although the thermal conductivity of solid paraffin is only 0.21 W/mK, it is still
490 much higher than that of air voids (0.025 W/mK). The improvement in thermal conductivity
491 could benefit the energy storage process. It should be mentioned that the thermal conductivity
492 of GPA-PCM is not only related to the bulk dry density but also the pore structure distribution.
493 Since there is a 10% volume change during the phase transition of PCM, the cavity caused by
494 the transition was different in cases of different pore structure distributions. The bulk dries
495 specific gravity of group 15S-0.35 (1.71) was similar to that of 15S-0.3-5B (1.69), while the

former had 12.74% higher thermal conductivity than the latter. This is because the latter group had more large pores and air voids compared to the former group. The larger pore structure provided a bigger cavity during the phase change, which reduced the thermal conductivity more significantly.

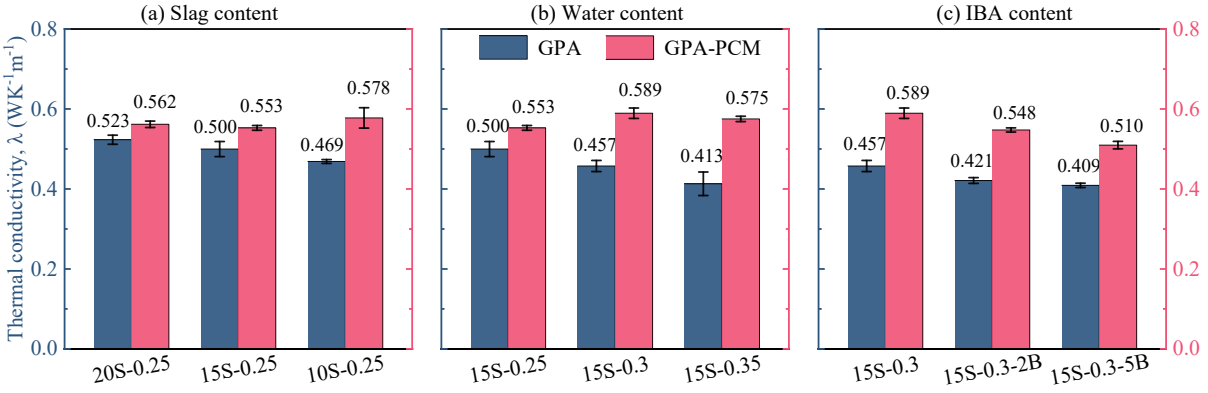

Fig. 14 Thermal conductivity of GPA and GPA-PCM affected by: (a) slag content; (b) water content; (3) IBA content.

3.3.4 Time-temperature history

Fig. 15a-c shows the time-temperature history curves of GPA and GPA-PCM, which describe the thermal regulation performance of GPA-PCM during the heating and cooling process. The temperature difference achieved by PCM in the produced GPA-PCM is presented in Fig. 15d. All these samples were heated via light bulbs for 60 minutes and then allowed for natural cooling for 90 minutes.

During the heating process, the peak inner temperature of all samples was quite similar at around 51°C and the thermal response of GPA-PCM could be divided into two stages based on the slope of the curves. The initial thermal response in GPA-PCM was slower than that in GPA. This is because the PCM impregnated in the GPA-PCM could absorb the thermal energy transferred into the thermocouples. Besides, since the thermal conductivity of paraffin is much lower than that of the geopolymer matrix, the thermal conduction process was affected by the PCM around the thermocouples. More importantly, the phase transition of PCM from solid to

liquid led to the pore structure redistribution, the change of thermal conductivity, and thus the heat transfer process of GPA-PCM. According to Fig. 15d, the ending of the first charging stage occurred within less than 15 minutes and depended on the PCM content in GPA-PCM. The higher PCM content led to a longer duration of this stage and a larger temperature difference. The temperature difference could achieve the highest value of 10.5°C in 15S-0.35 and the lowest value of 3.1°C in 20S-0.25. After the first stage, the temperature of GPA-PCM rapidly increased and gradually closed the gap with that of GPA due to the increase of thermal conductivity and more heat flow from the surrounding.

After the heating stage, these samples were allowed for natural cooling. The cooling process of GPA-PCM also exhibited two stages of thermal response. The first period was completed at around 85–95 minutes, as shown in the time-temperature history curves (Fig.15). During this period, all these samples showed similar thermal responses regardless of their mixture composition or presence of PCM. When the temperature of the aggregates reached around the crystallization temperature of GPA-PCM, as shown in Table 3, the liquid paraffin started to convert into a solid phase and release thermal energy, as marked by the slighter decrease of inner temperature compared with GPA. Compared with the charging process, the release of thermal energy was mild and lasted longer. Besides, due to the leakage of PCM during the heating process, the thermal regulation performance of GPA-PCM declined in the cooling process. It is shown that this releasing process was affected by the pore structure and PCM content. According to Fig. 15d, 15S-0.3-5B achieved the best performance in releasing the thermal energy while there was no obvious temperature difference in 20S-0.25 during the discharging process. Further work is needed to understand the mechanisms involved in the charging and discharging processes of GPA-PCM.

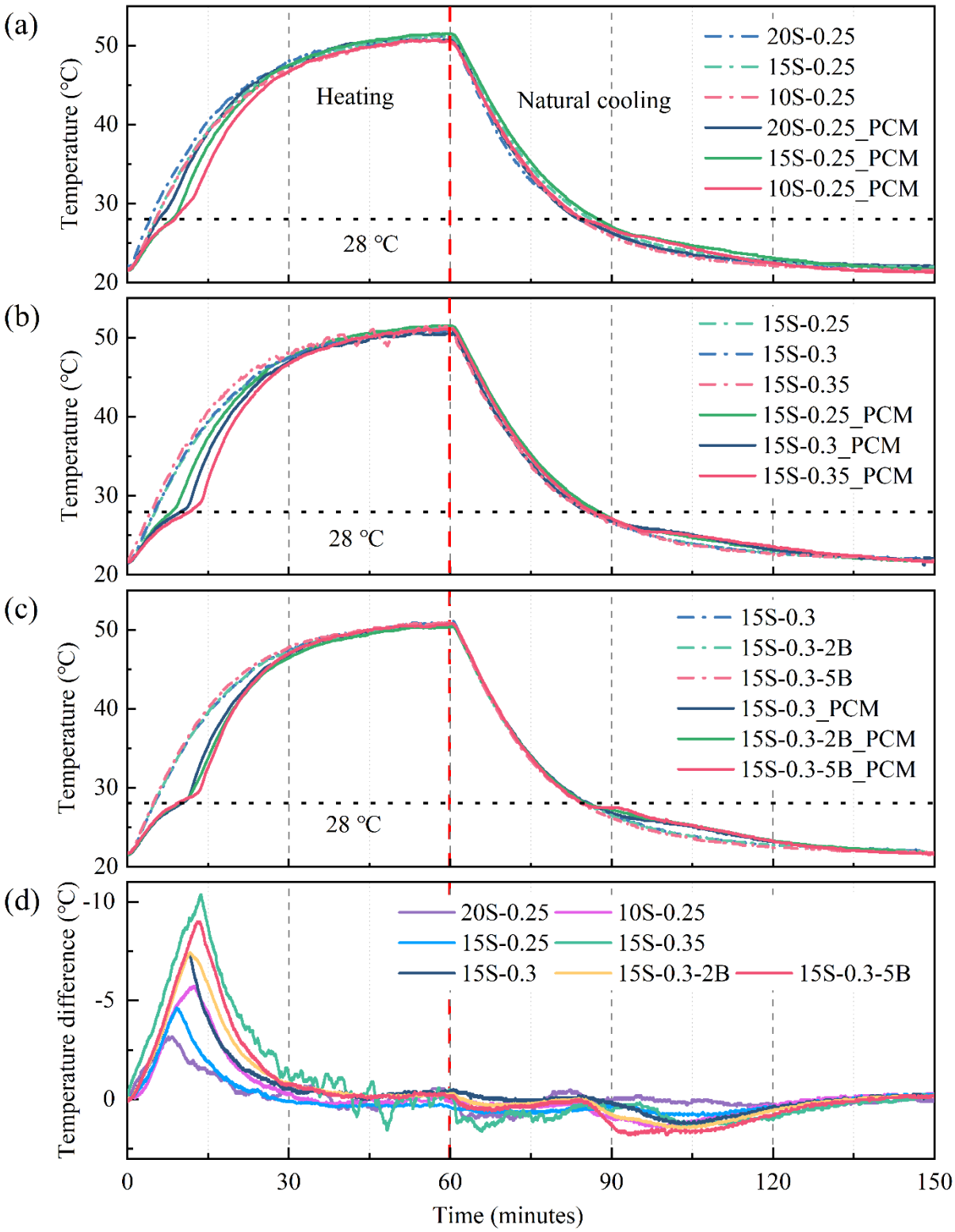

Fig. 15 Time-temperature history curves of GPA and GPA-PCM: (a) Effect of slag content; (b) Effect of water binder ratio; (c) Effect of IBA content; and (d) Temperature difference achieved by PCM.

3.4 Microstructure of GCA-PCM composites

The microstructure in 15S-0.5-5B (GPA) and 15S-0.5-5B-PCM (GPA-PCM) was investigated by micro-CT, and the 3D segmentation results are presented in Fig. 16. As shown in Fig. 16a, the volume of pores identified by the micro-CT in GPA was 18.16%, which verified the highly porous nature of produced GPA. Besides these large pores, a large number of capillary pores and gel pores could not be identified due to the relatively low resolution (14 μm) of this technique. For the group impregnated with PCM, the results of micro-CT are presented in Fig. 16b. The total identifiable porosity (including PCM and pores volume) was 18.08% by total volume, which is consistent with the results in GPA without PCM impregnation. This indicates the vacuum impregnation process had a negligible influence on larger size pores (≥ 14 μm). Out of the 18.08% pore volume, PCM occupied 15.18%, indicating a high absorption efficiency of 83.96% by volume. The remaining 2.90% porosity was associated with the presence of isolated pores and volume changes of PCM. When the paraffin changed its phase from solid to liquid at the phase change temperature, a large amount of energy was released, causing the volumetric expansion of PCM by 16.7%, which could fill the identifiable pores and further improve the absorption efficiency of PCM to 92.36%. Such a high value in the utilization rate of pores indicates an excellent application potential of GPA-PCM.

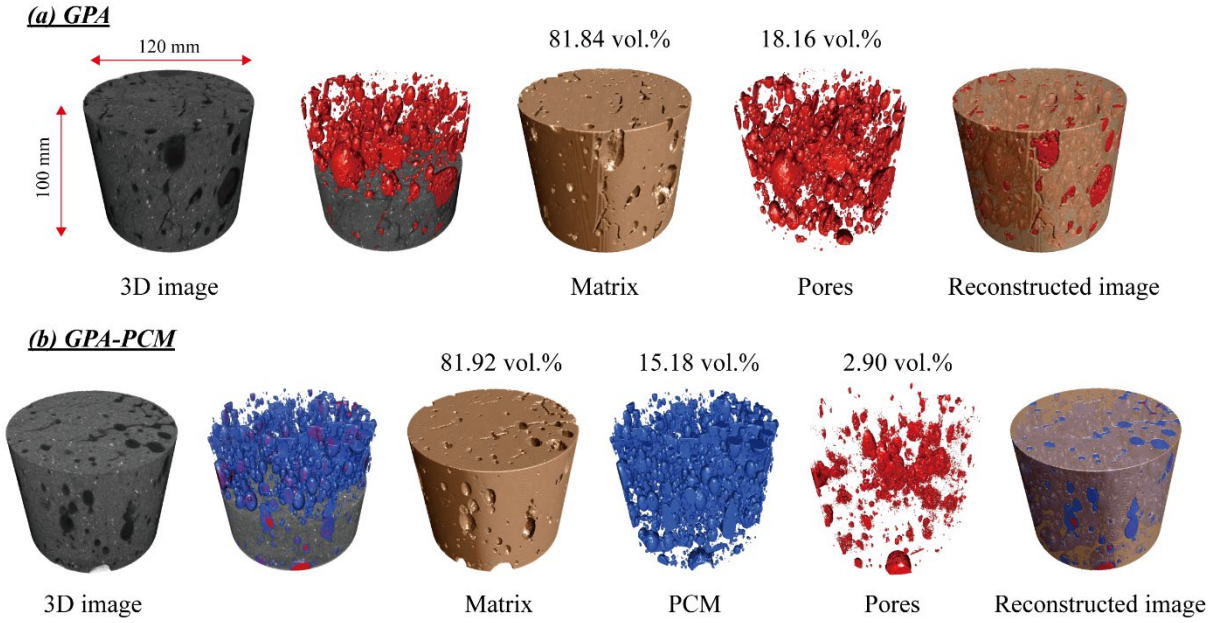

Fig. 16 Segmentation of microstructure in GPA and GPA-PCM for the group 15S-0.5-5B via micro-CT technology.

3.5 Environmental impacts assessment of GPA

Table 4 presents the estimated embodied carbon footprint and costs of the raw materials used in the production of GPA. All of the material costs are provided based on the laboratory supply list and previous research [25]. Here the use of IBA is assumed to generate zero carbon footprint because it consumes hazardous solid waste that brings a positive effect on the environment. Fig. 17 illustrates the embodied carbon footprint of produced GPA with different mix proportions, where the embodied carbon of other types of lightweight aggregates previously reported in the literature as PCM carriers, including expanded perlite [51], expanded clay [52], expanded foam glass [52], ceramic foam [53], and synthetic zeolite [54] is also presented for comparison.

It seems that the embodied carbon of produced GPA with different mix proportions varied slightly from 0.142 to 0.155 $kgCO_2e/kg$ since Na_2SiO_3-anhydrous is the main contributor to the carbon footprint in GPA. Compared with existing lightweight aggregates used for PCM carriers like expanded perlite and synthetic zeolite, GPA achieved a significant reduction of

581 embodied carbon by up to 72.69%. Besides, the production of GPA in fact can avoid the
582 exploitation of natural aggregates and reutilize the industry by-products such as fly ash and
583 GGBS, while in the meantime. All the above-mentioned benefits make the GPA a sustainable
584 and environmental-friendly solution.

585 The carbon emission of the preparation and crushing processes for natural aggregates was
586 around 0.00618 kgCO2e/kg [55]. However, the crushing energy of GPA is far lower than that
587 of natural aggregates due to the much lower compressive strength of the former (less than 5
588 MPa) at the crushing time, which indicates negligible carbon emissions. The energy of the
589 curing process could be calculated according to the following process. The energy consumption
590 required for curing can be calculated using the following equations [56]:

591 $$E_t = A v \rho_a C_a \Delta T t \quad (7)$$

592 where E_t is the total energy consumption (kWh); A is the cross-sectional area of container (1
593 m^2); υ is air velocity (0.5 m/s); ρ_a is air density (0.8986 kg/m^3); t is total drying time (24 h); ΔT
594 is the temperature difference (80 °C); and C_a is specific heat of the sample (0.657 kJ/kg °C)
595 [57].

596 The total energy consumption is therefore given as 283.38 kWh and the energy consumed
597 for drying per kilogram of GPA is calculated using:

598 $$E_{kg} = E_t / W_0 \quad (8)$$

599 where E_{kg} is specific energy required (0.708 kWh/kg) and W_0 is the initial weight of sample
600 (volume × bulk unit weight = 0.5 m^3 × 800 kg/m^3 = 400 kg for industrial production).

601 In addition, since the emission factor for the energy consumption could be 0.231
602 kgCO_2e/kWh [58], the carbon emission for the curing process could be calculated and the result
603 was 0.164 kgCO_2e/kg. Even though the carbon emission for the curing process itself was higher
604 than the embodied carbon of raw materials, this part of energy could be compensated by the
605 biomethane, biofuel, and waste heat steam from wet waste plants and waste incineration plants.

In addition, this accelerated curing method can improve the strength and quality of the aggregates and speed up the production efficiency, thus adding additional economic and environmental benefits.

The material cost of produced GPA was summarized in Fig. 18. It can be seen that the material cost of the produced GPA varied slightly from 549 to 571 CNY/metric ton. The main cost of GPA came from FA and alkaline activators. However, a number of researchers have explored various waste-derived alternative precursors [59] and activators [60] to produce more eco-friendly geopolymer. It should be highlighted that using artificial aggregates is motivated by the desire to solve three problems at once: (1) recycling industrial solid waste like fly ash, red mud, glass waste, calcium carbide residue, and so on, (2) immobilization of toxic waste like IBA, and (3) limiting the depletion of natural aggregates. The potential use of various waste materials in GPA can reduce the cost of waste treatment. In addition to the environmental benefits of GPA, it is anticipated that, in the future, the cost difference between the GPA and natural aggregates will be reduced with continued development of alternative alkali materials [25].

Table 4 Embodied carbon footprint and materials costs of raw materials

Materials	Fly ash	GGBS	Na_2SiO_3-Anhydrous	IBA	Water
Embodied carbon ($kgCO_2e/kg$)	0.008 [25]	0.083 [52]	1.860 [25]	0	0.001 [25]
Material costs (CNY/metric ton)	350	400	4100	0	4

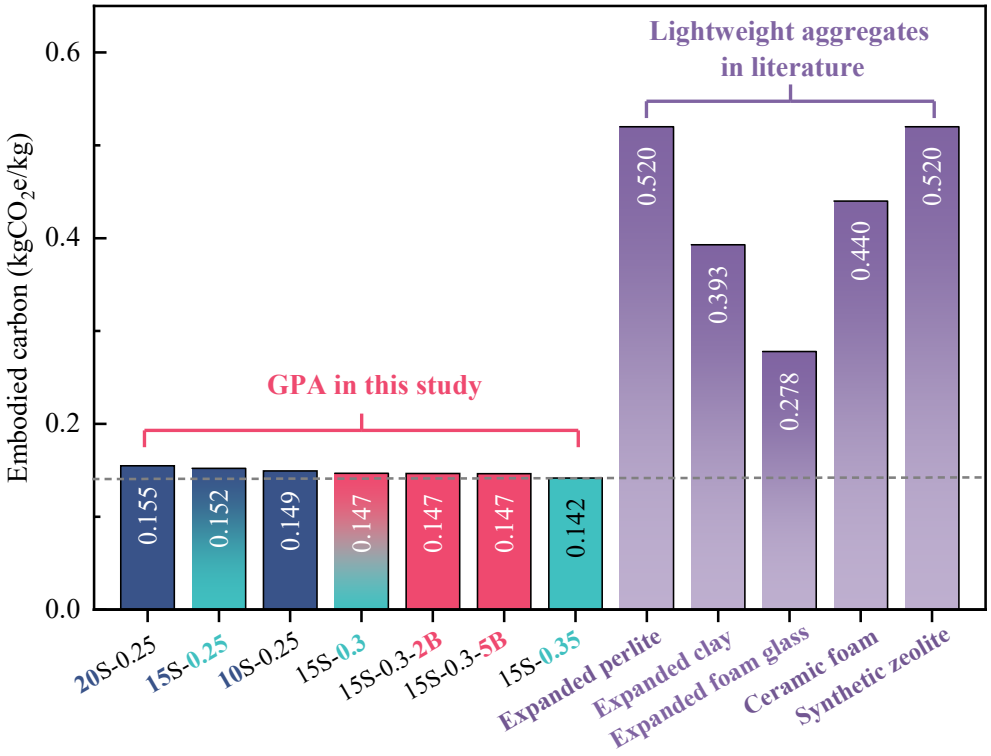

Fig. 17 Comparison of embodied carbon footprint between GPA and other lightweight aggregates as PCM carriers.

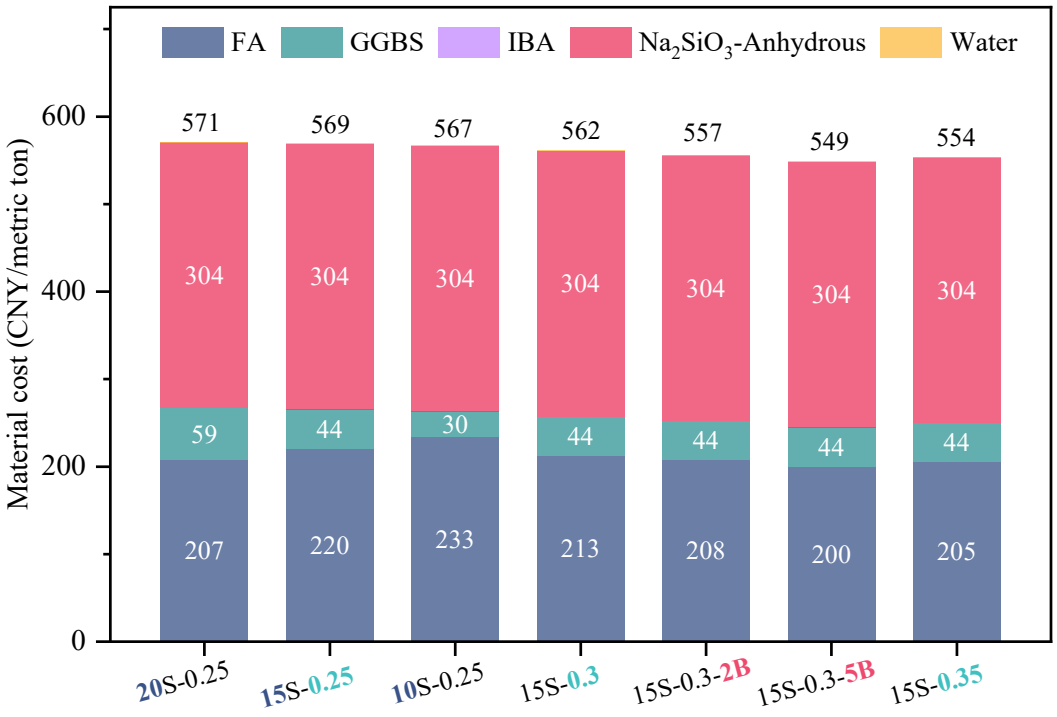

Fig. 18 Material costs of produced GPA.

4 Conclusions

This paper has conducted a comprehensive investigation into the feasibility of employing artificial geopolymer aggregate (GPA) as a novel shape-stabilized PCM carrier. The following conclusions have been reached through the investigations:

- Introducing IBA into the mix of GPA proved to be an efficient means to increase its porosity. The formed lightweight GPA could have a low bulk density of 1.52~1.62 and higher water absorption of 18.7~21.0% while remaining with a high compressive strength of 36.4~60.2MPa. Besides, with the increase in water and IBA contents, the specific gravity of aggregates was reduced, whereas the water absorption and porosity of GPA were increased. The increase of slag content led to an opposite effect to these above properties.
- The crushing strength of GPA was significantly affected by the water, slag, and IBA contents. The higher porosity in the GPA led to a lower crushing strength. After encapsulation of GPA with PCM, the water absorption rate of the formed GPA-PCM was significantly reduced to around 5.50% due to the pore-filling effect and the hydrophobic property of paraffin. The PCM could be absorbed into the GPA up to 15.99 wt. %.
- The PCM impregnation process partially declined the crushing strength of GPA-PCM, ranging from 4.13% to 25.46% as compared to GPA. The higher strength of GPA led to more strength loss in GPA-PCM due to the dilatation stress associated with the phase transformation. However, the crushing strength of GPA-PCM was still in the desirable range of 53.2 - 71.3 MPa.
- The GPA-PCM composites had good thermal stability and a considerable melting enthalpy of approximately 4.29 – 24.74 J/g. The thermal conductivity of GPA-PCM varied from 0.510 to 0.589 W/mK, which was higher than that of GPA. All the produced GPA-PCM fulfilled the criterion of insulation material.

- The produced GPA-PCM specimens showed very effective charging and discharging performance in the time-temperature history curves, leading to temperature regulation up to 10.5°C.
- The produced GPA exhibited a lower carbon footprint than other lightweight aggregates specified in existing literature as the PCM carrier.

CRediT authorship contribution statement

Yi Fang: Methodology, Investigation, Visualization, Writing – original draft. **Muhammad Riaz Ahmad**: Investigation, Writing-reviewing, and Editing. **Jian-Cong Lao**: Investigation. **Lan-Ping Qian**: Investigation, Resources. **Jian-Guo Dai**: Conceptualization, Funding acquisition, Supervision, Writing-reviewing, and Editing.

Declaration of competing interest

The authors declare that they have no known competing financial interests or personal relationships that could have appeared to influence the work reported in this paper.

Acknowledgments

The authors would like to acknowledge the financial support received from NSFC/RGC Joint Research Scheme (N_PolyU542/20), Hong Kong RGC General Research Fund (No. 15223120), and Research Centre for Resources Engineering towards Carbon Neutrality (No. BBC7).

References

[1] U.G. Compact, G.R. Initiative, SDG Compass: The guide for business action on the SDGs, (2015).

[2] Y. Konuklu, M. Ostry, H.O. Paksoy, P. Charvat, Review on using microencapsulated phase change materials (PCM) in building applications, Energy Build., 106 (2015) 134-155.

[3] H. Liu, X. Wang, D. Wu, Innovative design of microencapsulated phase change materials for thermal energy storage and versatile applications: a review, Sustainable Energy Fuels, 3(5) (2019) 1091-1149.

682 [4] Y. Zhang, G. Zhou, K. Lin, Q. Zhang, H. Di, Application of latent heat thermal energy
683 storage in buildings: State-of-the-art and outlook, Build. Environ., 42(6) (2007) 2197-
684 2209.

685 [5] N. Zhu, Z. Ma, S. Wang, Dynamic characteristics and energy performance of buildings
686 using phase change materials: a review, Energy Convers. Manage., 50(12) (2009) 3169-
687 3181.

688 [6] W.A. Qureshi, N.-K.C. Nair, M.M. Farid, Impact of energy storage in buildings on
689 electricity demand side management, Energy Convers. Manage., 52(5) (2011) 2110-
690 2120.

691 [7] X. Wang, W. Li, Z. Luo, K. Wang, S.P. Shah, Design, characteristic and application of
692 phase change materials for sustainable and energy efficient buildings: A review, Energy
693 Build., (2022) 111923.

694 [8] K. Biswas, J. Lu, P. Soroushian, S. Shrestha, Combined experimental and numerical
695 evaluation of a prototype nano-PCM enhanced wallboard, Appl. Energy, 131 (2014)
696 517-529.

697 [9] K. Roth, D. Westphalen, J. Brodrick, PCM technology for building materials, ASHRAE
698 J., 49(7) (2007) 129-132.

699 [10] A. Al-Ahmed, M.A.J. Mazumder, B. Salhi, A. Sari, M. Afzaal, F.A. Al-Sulaiman,
700 Effects of carbon-based fillers on thermal properties of fatty acids and their eutectics as
701 phase change materials used for thermal energy storage: A Review, J. Energy Storage,
702 35 (2021) 102329.

703 [11] M. Hunger, A. Entrop, I. Mandilaras, H. Brouwers, M. Founti, The behavior of self-
704 compacting concrete containing micro-encapsulated phase change materials, Cem.
705 Concr. Compos., 31(10) (2009) 731-743.

706 [12] A. Sari, M. Akcay, M. Soylak, A. Onal, Polymer-stearic acid blends as form-stable
707 phase change material for thermal energy storage, (2005).

708 [13] S. Cunha, M. Lima, J.B. Aguiar, Influence of adding phase change materials on the
709 physical and mechanical properties of cement mortars, Constr. Build. Mater., 127
710 (2016) 1-10.

711 [14] A. Sarı, Form-stable paraffin/high density polyethylene composites as solid–liquid
712 phase change material for thermal energy storage: preparation and thermal properties,
713 Energy Convers. Manage., 45(13-14) (2004) 2033-2042.

714 [15] M.M. Kenisarin, K.M. Kenisarina, Form-stable phase change materials for thermal
715 energy storage, Renewable Sustainable Energy Rev., 16(4) (2012) 1999-2040.

716 [16] K. Kaygusuz, C. Alkan, A. Sari, O. Uzun, Encapsulated fatty acids in an acrylic resin as
717 shape-stabilized phase change materials for latent heat thermal energy storage, Energy
718 Sources, Part A, 30(11) (2008) 1050-1059.

[17] K. Yuan, Y. Zhou, W. Sun, X. Fang, Z. Zhang, A polymer-coated calcium chloride hexahydrate/expanded graphite composite phase change material with enhanced thermal reliability and good applicability, Compos. Sci. Technol., 156 (2018) 78-86.

[18] T. Li, Y. Yuan, N. Zhang, Thermal properties of phase change cement board with capric acid/expanded perlite form-stable phase change material, Adv. Mech. Eng., 9(6) (2017) 1687814017701706.

[19] W. Liao, A. Kumar, K. Khayat, H. Ma, Multifunctional Lightweight Aggregate Containing Phase Change Material and Water for Damage Mitigation of Concrete, ES Materials & Manufacturing, 6 (2019) 49-61.

[20] J. Choi, V. Valtchev, T. Moteki, M. Ogura, Phase Change Material-Containing Mesoporous Zeolite Composite for Adsorption Heat Recovery, Adv. Mater. Interfaces, 8(4) (2021) 2001085.

[21] Y. Li, J. Li, Y. Deng, W. Guan, X. Wang, T. Qian, Preparation of paraffin/porous TiO2 foams with enhanced thermal conductivity as PCM, by covering the TiO2 surface with a carbon layer, Appl. Energy, 171 (2016) 37-45.

[22] A. Yousefi, W. Tang, M. Khavarian, C. Fang, Development of novel form-stable phase change material (PCM) composite using recycled expanded glass for thermal energy storage in cementitious composite, Renewable Energy, 175 (2021) 14-28.

[23] T. Khadiran, M.Z. Hussein, Z. Zainal, R. Rusli, Encapsulation techniques for organic phase change materials as thermal energy storage medium: A review, Sol. Energy Mater. Sol. Cells, 143 (2015) 78-98.

[24] L.-P. Qian, L.-Y. Xu, Y. Alrefaei, T. Wang, T. Ishida, J.-G. Dai, Artificial alkali-activated aggregates developed from wastes and by-products: A state-of-the-art review, Resour. Conserv. Recycl., 177 (2022) 105971.

[25] L. Xu, L. Qian, B. Huang, J. Dai, Development of artificial one-part geopolymer lightweight aggregates by crushing technique, J. Cleaner Prod., 315 (2021) 128200.

[26] L.-Y. Xu, B.-T. Huang, V.C. Li, J.-G. Dai, High-strength high-ductility Engineered/Strain-Hardening Cementitious Composites (ECC/SHCC) incorporating geopolymer fine aggregates, Cem. Concr. Compos., 125 (2022) 104296.

[27] L.-Y. Xu, B.-T. Huang, J.-G. Dai, Development of engineered cementitious composites (ECC) using artificial fine aggregates, Constr. Build. Mater., 305 (2021) 124742.

[28] X. Qiao, M. Tyrer, C.S. Poon, C.R. Cheeseman, Characterization of alkali-activated thermally treated incinerator bottom ash, Waste Manage. (Oxford), 28(10) (2008) 1955-1962.

[29] ASTM, C618-19: Standard specification for coal fly ash and raw or calcined natural pozzolan for use in concrete, ASTM international, West Conshohocken, PA, 2019.

[30] Y. Alrefaei, Y.-S. Wang, J.-G. Dai, The effectiveness of different superplasticizers in ambient cured one-part alkali activated pastes, Cem. Concr. Compos., 97 (2019) 166-174.

[31] ASTM, C128-15: Standard Test Method for Relative Density (Specific Gravity) and Absorption of Fine Aggregate, West Conshohocken, PA, 2015.

[32] ASTM, C127-15: Standard Test Method for Relative Density (Specific Gravity) and Absorption of Coarse Aggregate, West Conshohocken, PA, 2015.

[33] R. Qian, J. Shi, C. Liu, G. Liu, Z. Liu, W. She, Y. Zhang, Y. Zhang, Y. Liang, Investigations on pore-structure in cementitious materials using gas intrusion porosimetry, Measurement, 171 (2021) 108816.

[34] ASTM, ASTM C109/C109M: Standard Test Method for Compressive Strength of Hydraulic Cement Mortars, West Conshohocken, PA, 2021.

[35] B.-T. Huang, J.-X. Zhu, K.-F. Weng, V.C. Li, J.-G. Dai, Ultra-high-strength engineered/strain-hardening cementitious composites (ECC/SHCC): Material design and effect of fiber hybridization, Cem. Concr. Compos., 129 (2022) 104464.

[36] K. Scrivener, R. Snellings, B. Lothenbach, A practical guide to microstructural analysis of cementitious materials, CRC Press Taylor & Francis Group, Boca Raton, 2016.

[37] M. Wagner, Thermal Analysis in Practice: Fundamental Aspects, Carl Hanser Verlag GmbH Co KG2018.

[38] I. Asadi, P. Shafigh, Z.F.B.A. Hassan, N.B. Mahyuddin, Thermal conductivity of concrete–A review, J. Build. Eng., 20 (2018) 81-93.

[39] M.R. Ahmad, B. Chen, Experimental research on the performance of lightweight concrete containing foam and expanded clay aggregate, Composites, Part B, 171 (2019) 46-60.

[40] W. Liao, C. Zeng, Y. Zhuang, H. Ma, W. Deng, J. Huang, Mitigation of thermal curling of concrete slab using phase change material: A feasibility study, Cem. Concr. Compos., 120 (2021) 104021.

[41] B. Xu, Z. Li, Paraffin/diatomite composite phase change material incorporated cement-based composite for thermal energy storage, Appl. Energy, 105 (2013) 229-237.

[42] C. Atiş, E. Görür, O. Karahan, C. Bilim, S. İlkentapar, E. Luga, Very high strength (120 MPa) class F fly ash geopolymer mortar activated at different NaOH amount, heat curing temperature and heat curing duration, Constr. Build. Mater., 96 (2015) 673-678.

[43] P. Nath, P.K. Sarker, Effect of GGBFS on setting, workability and early strength properties of fly ash geopolymer concrete cured in ambient condition, Constr. Build. Mater., 66 (2014) 163-171.

[44] S. Samantasinghar, S.P. Singh, Effect of synthesis parameters on compressive strength of fly ash-slag blended geopolymer, Constr. Build. Mater., 170 (2018) 225-234.

[45] Z.P. Bažant, Size effect on structural strength: a review, Archive of applied Mechanics, 69(9) (1999) 703-725.

794 [46] X. Zhang, X. Li, Y. Zhou, C. Hai, Y. Shen, X. Ren, J. Zeng, Calcium Chloride
795 Hexahydrate/Diatomite/Paraffin as Composite Shape-Stabilized Phase-Change Material
796 for Thermal Energy Storage, Energy & Fuels, 32(1) (2018) 916-921.

797 [47] H. Li, H. Chen, X. Li, J.G. Sanjayan, Development of thermal energy storage
798 composites and prevention of PCM leakage, Appl. Energy, 135 (2014) 225-233.

799 [48] G.W. Scherer, Freezing gels, J. Non-Cryst. Solids, 155(1) (1993) 1-25.

800 [49] O. Gencel, G. Hekimoğlu, A. Sarı, M. Sutcu, Y. Er, A. Ustaoglu, A novel energy-
801 effective and carbon-emission reducing mortars with bottom ash and phase change
802 material: Physico-mechanical and thermal energy storage characteristics, J. Energy
803 Storage, 44 (2021) 103325.

804 [50] L. Rilem, Functional classification of lightweight concrete, Materials and Structures, 11
805 (1978) 281-283.

806 [51] G. Hammond, C. Jones, Embodied Carbon: The Inventory of Carbon and Energy (ICE),
807 BSRIA Guide BG 10/2011, Building Services Research and Information Association:
808 Berkshire, (2011).

809 [52] G. Hammond, C. Jones, Inventory of carbon & energy (ICE) version 3.0, University of
810 Bath, (2019).

811 [53] Z. Zimele, M. Sinka, A. Korjakins, D. Bajare, G. Sahmenko, Life Cycle Assessment of
812 Foam Concrete Production in Latvia, Environmental & Climate Technologies, 23(3)
813 (2019).

814 [54] P. Tobarameekul, P. Worathanakul, Heat Management Options to Reduce Carbon
815 Footprint of Green Zeolite Faujasite Synthesis from Rice Husk Ash, Thai
816 Environmental Engineering Journal, 35(3) (2021) 59-68.

817 [55] NSSGA, The Aggregates Industry Greenhouse Gases: Low Emissions, High Resiliency,
818 Alexandria, VA, 2021.

819 [56] A. Motevali, S. Minaei, M.H. Khoshtagaza, Evaluation of energy consumption in
820 different drying methods, Energy Convers. Manage., 52(2) (2011) 1192-1199.

821 [57] F. Cardarelli, Materials handbook: a concise desktop reference, Springer-Verlag,
822 London, 2008.

823 [58] M. Kumar, S. Prashant, M.V. Kamath, Enhancing the sustainability of high strength
824 concrete in terms of embodied energy and carbon emission by incorporating sewage
825 sludge and fly ash, Innovative Infrastructure Solutions, 7(4) (2022) 240.

826 [59] F. Mobasheri, S. Mirvalad, A.A. Shirzadi Javid, S. Azizi, M. Ghoroqi, Waste glass as a
827 precursor in alkali-activated materials: Mechanical, durability, and microstructural
828 properties, Struct. Concr., (2022).

829 [60] B.C. Mendes, L.G. Pedroti, C.M.F. Vieira, M. Marvila, A.R. Azevedo, J.M.F. de
830 Carvalho, J.C.L. Ribeiro, Application of eco-friendly alternative activators in alkali-
831 activated materials: A review, J. Build. Eng., 35 (2021) 102010.